



Peroxymonosulfate enhanced visible light photocatalytic degradation bisphenol A by single-atom dispersed Ag mesoporous g-C₃N₄ hybrid

Yanbin Wang^a, Xu Zhao^{a,b,*}, Di Cao^{a,b}, Yan Wang^a, Yongfa Zhu^c

^a Key Laboratory of Drinking Water Science and Technology, Research Center for Eco-Environmental Sciences, Chinese Academy of Sciences, Beijing, 100085, PR China

^b University of Chinese Academy of Sciences, Beijing, 100049, PR China

^c Department of Chemistry, Beijing Key Laboratory for Analytical Methods and Instrumentation, Tsinghua University, Beijing, 100084, PR China

ARTICLE INFO

Article history:

Received 6 February 2017

Received in revised form 27 March 2017

Accepted 31 March 2017

Available online 8 April 2017

Keywords:

Graphitic carbon nitride

Single-atom silver

Peroxymonosulfate

Photocatalysis

Sulfate radical

ABSTRACT

Single-atom dispersed Ag modified mesoporous graphitic carbon nitride (Ag/mpg-C₃N₄) hybrid was synthesized by co-condensation method and employed as a visible light photocatalyst. In the presence of peroxymonosulfate (PMS), Ag/mpg-C₃N₄ showed excellent performance for the degradation of bisphenol A (BPA). 100% BPA and 80% TOC could be removed with 0.1 g/L catalyst and 1 mM PMS under visible light ($\lambda > 400$ nm) within 60 min. The reason for the enhanced performance is possibly due to the synergistic effect of single-atom Ag and mpg-C₃N₄. On the one hand, more visible light could be captured with the introduction of Ag; on the other hand, the existence of PMS promotes the separation efficiency of photogenerated electron-hole pairs. Electron spin resonance (ESR) and free radicals quenching experiment suggest that the major reactive oxygen species (ROS) are sulfate radical (SO₄^{•−}), superoxide radicals (O₂^{•−}) and photogenerated holes, while the role of hydroxyl radicals (•OH) is insignificant in this process. The findings of this work highlighted the great potential of g-C₃N₄ as photocatalysts and elucidated a new opportunity for PMS remediation of contaminated water.

© 2017 Elsevier B.V. All rights reserved.

1. Introduction

Graphitic carbon nitride (g-C₃N₄), as a metal-free polymeric semiconductor, has shown huge potential in the field of photocatalytic H₂ evolution [1–3], CO₂ reduction [4,5], contamination elimination [6,7], and H₂O₂ synthesis [8–10]. With an optical band gap of 2.70 eV, g-C₃N₄ has shown a response to visible light up to 460 nm. Nevertheless, the photocatalytic performance of g-C₃N₄ is restricted by the low quantum efficiency originated from its slow charge mobility and fast recombination of photogenerated electron-hole pairs. To overcome the above mentioned disadvantages, various strategies have been developed to improve the photocatalytic performance of g-C₃N₄, such as constructing heterojunctions [11,12], doping with non-metal [13–16] or noble metal [17], modifying with inorganic or organic semiconductors [18]. The photocatalytic activity of semiconductors could be significantly improved by modifying with noble metal (Ag, Au and Pt), resulting from the surface plasmon resonance (SPR) effect. It is reported

that the noble metal particles could act as electron sinks, trapping free electron and thereby reducing the recombination rate of photogenerated electron-hole [17].

Recently, single-atom catalysis has become a research hotspot, because in single-atom catalysts atom efficiency can be maximized. The cooperation of single-atom noble metals into g-C₃N₄ provides a new strategy to modulate the electronic structure of g-C₃N₄, resulting in a longer lifetime of photogenerated electrons. For example, Li et al. [19] reported single-atom Pt as co-catalyst of g-C₃N₄ for photocatalytic H₂ evolution, and its performance was 8.6 times higher than that of Pt nanoparticles and 50 times higher than that of bare g-C₃N₄. Gao et al. [20] studied single-atom Pd and Pt supported on g-C₃N₄ for CO₂ reduction by density functional theory calculations, and the single-atom photocatalyst showed excellent activity for CO₂ reduction. Chen et al. [21] synthesized a single-atom dispersed Ag/g-C₃N₄ catalyst via copolymerization with silver tricyanomethanide and cyanamide, which showed an enhanced performance in the selective hydrogenation of alkynes in comparison with other conventional Ag-based materials.

The photocatalytic performance can also be tremendously enhanced with the addition of oxidants such as H₂O₂, persulfate (PS) and peroxymonosulfate (PMS). The oxidants are activated by the photogenerated electrons to generate reactive species such as hydroxyl radical (•OH), superoxide radical (O₂^{•−}) and sulfate

* Corresponding author at: Key Laboratory of Drinking Water Science and Technology, Research Center for Eco-Environmental Sciences, Chinese Academy of Sciences, Beijing 100085, PR China.

E-mail address: zhaoxu@rcees.ac.cn (X. Zhao).

radical ($\text{SO}_4^{\bullet-}$), which can immediately destruct organic pollutants to CO_2 and H_2O . It is generally accepted that $\text{SO}_4^{\bullet-}$ has the potential of becoming an alternative to $\bullet\text{OH}$ (1.8–2.7 V vs. normal hydrogen electrode (NHE)) [22]. Compared with $\bullet\text{OH}$, $\text{SO}_4^{\bullet-}$ has a series of merits, such as stronger oxidizing capability (2.5–3.1 V vs. NHE), higher selectivity of oxidation and independence of pH [23]. For example, Gao et al. [24] found that the introduction of PS can be activated by photogenerated electrons to generate $\text{SO}_4^{\bullet-}$, resulting the accelerated photocatalytic degradation of AO7 in the MIL-53(Fe)/PS/vis process.

Inspired by these excellent works abovementioned, single-atom dispersed Ag mesoporous $\text{g-C}_3\text{N}_4$ hybrid ($\text{Ag/mpg-C}_3\text{N}_4$) was synthesized and applied as a photocatalyst to degrade BPA in the presence of PMS. The objectives of the present study were 1) to evaluate the photocatalytic performance of $\text{Ag/mpg-C}_3\text{N}_4$ in the presence of PMS, which may induce synergistic effects under visible light irradiation; 2) to investigate the effect of Ag contents, PMS concentration, initial pH and anion ions on the photocatalytic degradation of BPA; 3) to identify the generated reactive oxygen species (ROS) and charge transfer during photocatalytic process, and propose a plausible mechanism.

2. Experimental

2.1. Chemicals

Potassium tricyanomethanide (C_4KN_3) and cyanamide (CH_2N_2) were purchased from Alfa Aesar. Potassium peroxydisulfate (Oxone, $2\text{KHSO}_5 \cdot \text{KHSO}_4 \cdot \text{K}_2\text{SO}_4$) was purchased from Aladdin Chemistry Co. Ltd., China. 5-*tert*-Butoxycarbonyl-5-methyl-1-pyrroline-*N*-oxide (BMPO, 99.0%) was purchased from DOJINDO. Silver nitrate (AgNO_3), methanol (CH_3OH), *tert*-butyl alcohol ($\text{C}_4\text{H}_{10}\text{O}$), disodium ethylenediaminetetraacetate (EDTA-2Na), *p*-benzoquinone (*p*-BQ), sodium chloride (NaCl), sodium bicarbonate (NaHCO_3), sodium dihydrogen phosphate (NaH_2PO_4), sodium nitrate (NaNO_3), and sodium sulfate (Na_2SO_4) were obtained from Sinopharm Chemical Reagent Co., Ltd. Bisphenol A was obtained from TCI, Japan. All chemicals were used as received without any further purification. All solutions were prepared with Milli-Q water ($18.2 \text{ M}\Omega/\text{cm}$) produced on a Milli-Q purification system (Millipore, Billerica, MA).

2.2. Preparation and characterization of $\text{Ag/mpg-C}_3\text{N}_4$

The $\text{Ag/mpg-C}_3\text{N}_4$ photocatalysts were synthesized according to the previous literature [21] with slight modification. The typical preparation process as follows: 0.5 g potassium tricyanomethanide was dissolved into 12 mL H_2O (solution A), and 0.658 g AgNO_3 was dissolved into 18 mL H_2O (solution B). The two solutions were heated to 80°C with water bath. Then, the solution B was dropped into the solution A under vigorously stirring. After that, the flask was covered by Al foil and continuous stirred overnight at room temperature. The obtained precipitate was filtered and washed with deionized water, then dried under vacuum at 60°C . The samples were denoted as AgTCM. To obtain photocatalyst with different Ag contents, 1250 mg cyanamide and different mass of AgTCM (12.5, 25, 43.8, 62.5 and 125 mg) were dispersed into 2–3 mL H_2O , then adding 40% silica nanosphere ($\sim 40 \text{ nm}$ of diameter) suspension, maintaining the ratio of precursor to silica with 1:1. The mixture was stirred at 100°C for several hours to evaporate the water. The obtained white powder was fully grinding and heated to 550°C with the ramping rate of $2.3^\circ\text{C}/\text{min}$ under N_2 protection. Finally, the yellow powder were washed with $4 \text{ M NH}_4\text{HF}_2$ for 48 h to remove silica. After filtering and washing with H_2O and ethanol, the powders were dried under vacuum at 50°C , and were denoted

as 1%, 2%, 3.5%, 5% and 10% $\text{Ag/mpg-C}_3\text{N}_4$ according to the addition mass of AgTCM. The $\text{g-C}_3\text{N}_4$ as reference was obtained by a simple thermal polycondensation method. A certain amount of urea was put into crucible and heated in static air by a muffle furnace at 550°C for 4 h with heating rate of $5^\circ\text{C}/\text{min}$.

Field emission-scanning electron microscope (FE-SEM) was obtained using SU8010 (HITACHI, Japan). High resolution transmission electron microscopy (HRTEM) was performed on a JEM-2100F. X-ray diffraction (XRD) patterns were recorded on an X-ray diffractometer (X'pert Pro MPD) using $\text{Cu K}\alpha$ ($\lambda = 1.540 \text{ \AA}$). N_2 adsorption-desorption isotherms were applied to estimate the specific surface area, pore volume, and pore size distribution using ASAP2020 HD88 instrument (Micromeritics, USA) working at -196°C . Diffuse reflectance UV-vis spectra (UV-vis DRS) of the powder were obtained for the dry-pressed disk samples using UV-vis spectrometer (UV-2550, Shimadzu, Japan). The X-ray photoelectron spectroscopy (XPS) was measured on a photoelectron spectrometer (PHI Quantera SXM, ULVAC-PHI, Japan) with Al $\text{K}\alpha$ as the X-ray source. The XPS spectra were fitted with the CasaXPS software and the binding energy were calibrated to 284.6 eV .

2.3. Photoelectrochemical test

The photocurrent response, liner sweep voltammetry (LSV) and electrochemical impedance measurements were performed using a CHI660E electrochemical workstation (Chenhua Instrument Co. Ltd., Shanghai, China) with a standard three-electrode system. The working electrode was prepared as follows: 10 mg photocatalyst was dispersed in a mixture of 5% Nafion solution ($200 \mu\text{L}$) and ethanol ($800 \mu\text{L}$) and ultrasonicated for 180 min to form a uniform suspension. Then, $100 \mu\text{L}$ of suspension was dip-coated on the ITO and dried overnight at room temperature. The as-prepared electrode, Pt wire and saturated calomel electrode (SCE) were acted as working electrode, counter electrode and reference electrode, respectively. The working electrode was irradiated from the opposite side of the as-prepared film under a 300 W Xe lamp (PLS-SXE300; Perfect Light Co., Ltd, Beijing, China). Incident visible light was obtained by utilizing a 400 nm cutoff filter. 50 mM Na_2SO_4 aqueous solution was used as the electrolyte.

2.4. Batch experimental procedure

Photocatalytic experiments were carried out in a rectangular quartz reactor (120 mL , $50 \times 50 \times 50 \text{ mm}$). The initial pH value of 20 mg/L BPA was about 5.5. The pH values of solution were adjusted by 0.1 M H_2SO_4 and 0.1 M NaOH . 10 mg photocatalyst was added into the solution and stirred for 10 min to reach adsorption/desorption equilibrium between $\text{Ag/mpg-C}_3\text{N}_4$ and BPA. Then, a certain amount of PMS was added into the suspension and illuminated by Xe lamp (PLS-SXE300; Beijing Perfect Light Co., Ltd, Beijing, China) with a UV cutoff filter ($\lambda > 400 \text{ nm}$). At given time intervals, $500 \mu\text{L}$ samples were taken from the reactor and immediately mixed with $500 \mu\text{L}$ methanol, and filtered through a Millipore filter (pore size of $0.22 \mu\text{m}$) for HPLC analysis.

2.5. Analytical methods

The concentrations of BPA were analyzed by high performance liquid chromatography (HPLC; Shimadzu LC-20AT, Tokyo, Japan) equipped with a C18 column ($250 \text{ mm} \times 4.6 \text{ mm} \times 5 \mu\text{m}$, GL Science Inc., Tokyo, Japan) and a UV detector. The mobile phase was a mixture of methanol and water ($V/V = 70/30$) with a flow rate of $1 \text{ mL}/\text{min}$. The injection volume was set as $20 \mu\text{L}$. For electron spin resonance (ESR) measurement, $10 \mu\text{L}$ of the sample was collected from the suspension system and immediately mixed with $10 \mu\text{L}$ of 25 mM BMPO. ESR spectra were obtained on a Bruker EMX A300-

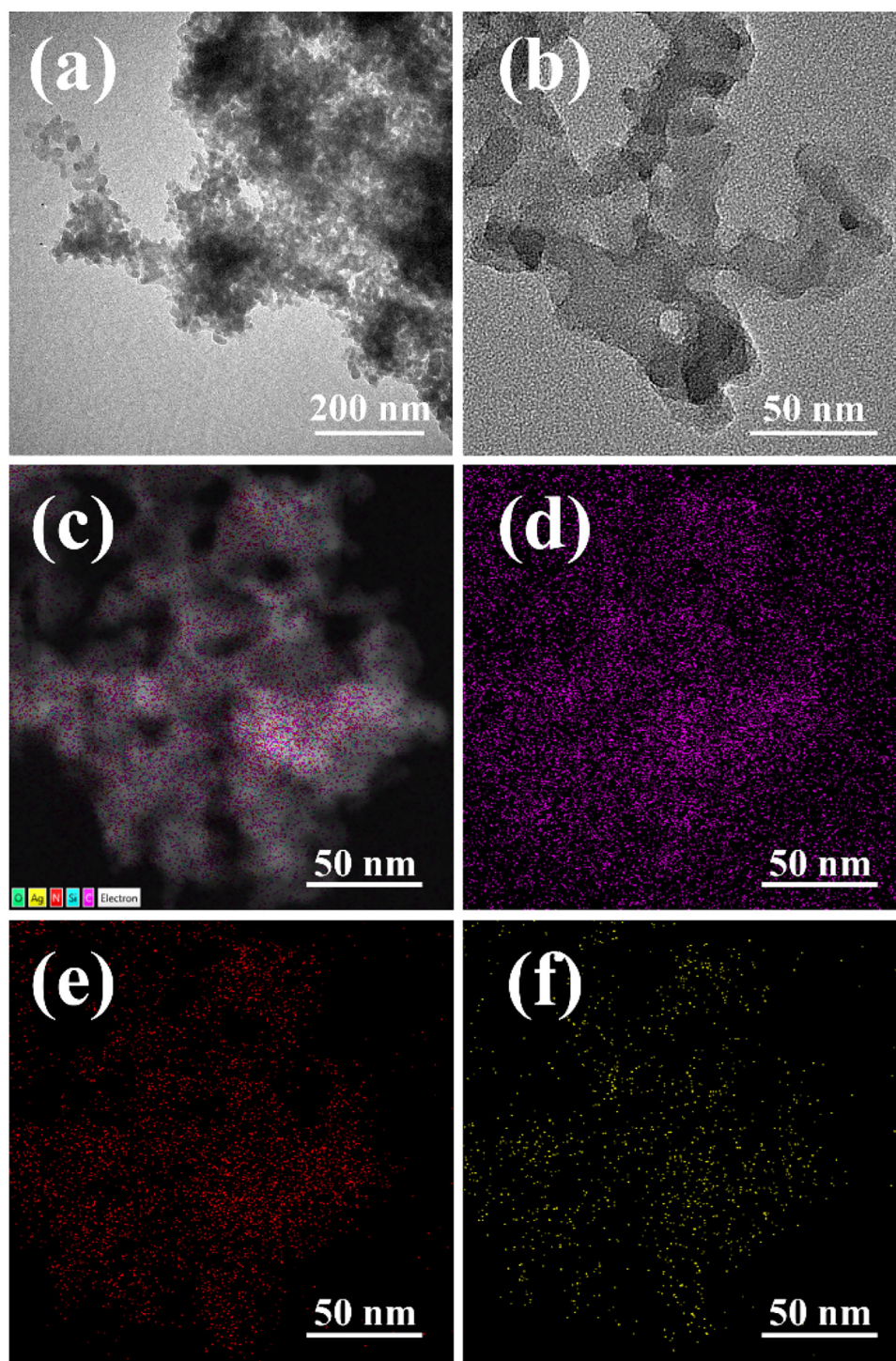


Fig. 1. TEM (a–b), STEM image (c), and EDX elemental mapping images of 10% Ag/mpg- C_3N_4 : carbon, (d), nitrogen (e) and silver (f). (For interpretation of the references to color in this figure legend, the reader is referred to the web version of this article.)

10/12 (Germany) with Microwave Bridge (microwave frequency, 9.85 GHz; microwave power, 22.8 mW; modulation amplitude, 1 G; modulation frequency, 100 kHz).

3. Results and discussion

3.1. Physicochemical property

SEM images of Ag/mpg- C_3N_4 with different Ag contents are shown in Fig. S1. It can be seen that mpg- C_3N_4 is composed

of uniform nanoparticles with diameters about 50 nm (Fig. S1a). The morphologies of Ag/mpg- C_3N_4 with different Ag contents are similar with mpg- C_3N_4 (Fig. S1b–f), which means the introduction of Ag does not change the morphology of mpg- C_3N_4 . The TEM images (Fig. 1a–b) indicate that 10% Ag/mpg- C_3N_4 possesses pore-like structure, which results from the reverse replication of silica nanosphere template. These porous structure will greatly enhance the specific surface area of g- C_3N_4 . No Ag nanoparticles are observed in the scanning transmission electron microscopy (STEM)

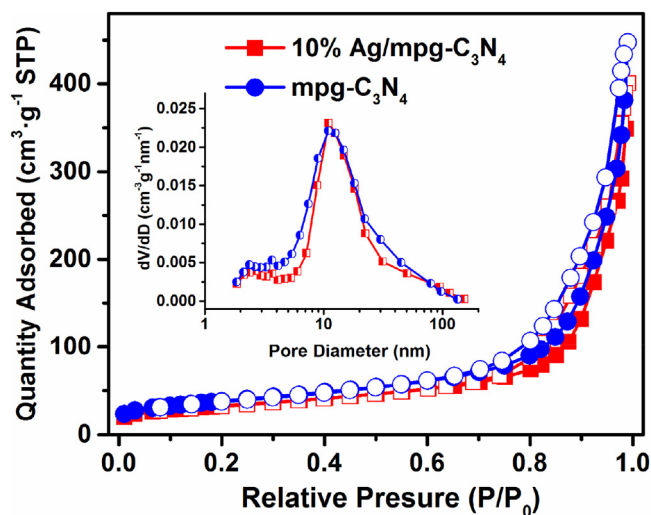


Fig. 2. N_2 adsorption-desorption isotherms of mpg- C_3N_4 and 10% Ag/mpg- C_3N_4 and the corresponding pore size distribution (inset).

image (Fig. 1c), and Ag homogeneously disperse in the matrix of mpg- C_3N_4 . It could be concluded that Ag is single-atom dispersed.

N_2 adsorption-desorption isotherms and the corresponding pore size distribution (inset) of mpg- C_3N_4 and 10% Ag/mpg- C_3N_4 are shown in Fig. 2. The isotherms exhibit a type IV curve with a H3 hysteresis loop, reflecting the mesoporous structure of the catalysts. The BET specific surface area of 10% Ag/mpg- C_3N_4 is $114 \text{ m}^2/\text{g}$, much higher than that of reported $\text{Ag}_2\text{O}/\text{g}-C_3N_4$ ($20.3 \text{ m}^2/\text{g}$) [25] and $\text{Ag}_3\text{PO}_4/\text{p}-\text{g}-C_3N_4$ ($0.2 \text{ m}^2/\text{g}$) [26]. The average pore size of 10% Ag/mpg- C_3N_4 is 19.7 nm, and the pore volume is $0.62 \text{ cm}^3/\text{g}$.

Fig. 3 shows the XRD patterns of Ag/mpg- C_3N_4 with different Ag contents. The peak at 27° corresponds to the (002) of g- C_3N_4 due to the interlayer-stacking, and the peak at 13° can be indexed to the (100) diffraction plane of g- C_3N_4 , corresponding to the in-plane structural packing motif [27]. It could be seen that the intensity of the peak at 27° decrease and the half peak width broaden with the increasing Ag contents, demonstrating slight disturbance of the local C_3N_4 network structure and the decrease of the crystallite size of g- C_3N_4 .

Fig. 4 shows the diffuse reflectance UV-vis spectra and Tauc plots of Ag/mpg- C_3N_4 with different Ag contents. As seen in Fig. 4a, the visible light absorption thresholds shift to longer wavelength with the Ag contents increasing. The enhanced absorption in the

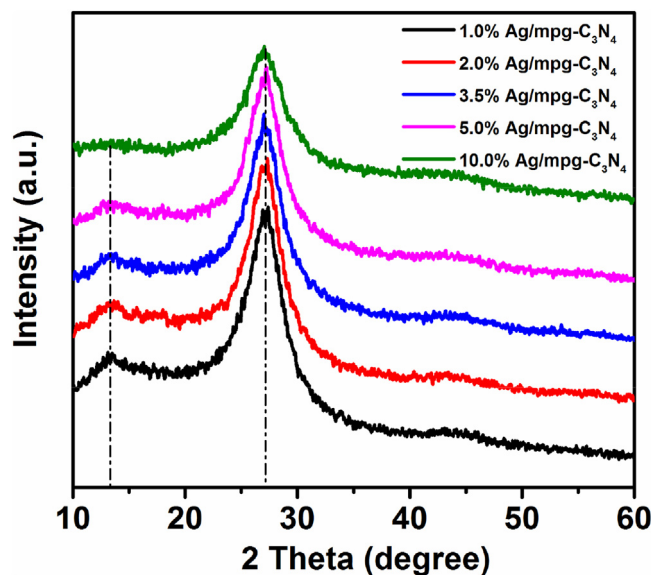


Fig. 3. The XRD patterns of Ag/mpg- C_3N_4 with different Ag contents.

visible light region is attributed to the characteristic SPR absorption of metallic Ag. The Tauc plot (Fig. 4b) of the absorption data reveal that the band gap energy of mpg- C_3N_4 is 2.50 eV, which is lower than that of 2.65 eV for g- C_3N_4 (Fig. S2). In addition, mpg- C_3N_4 shows stronger absorption at $\lambda < 400 \text{ nm}$ than g- C_3N_4 due to the multiple light scattering effects by the mesoporous structure [10]. The estimated band gap energies of 1%, 2%, 3.5%, 5% and 10% Ag/mpg- C_3N_4 are 2.50, 2.42, 2.39, 2.33 and 2.09 eV, respectively. It can be concluded that the existence of Ag benefits of the absorption of visible light. It has been reported that the conduction band of g- C_3N_4 is about -1.3 V (vs. NHE) [9]. Ag possesses a favorable Fermi level (0.4 V vs. NHE) [28], and can serve as a good electron acceptor. Therefore, the photogenerated electrons on conduction band of g- C_3N_4 can be quickly transfer to Ag, reusing in the narrow band gap of Ag/mpg- C_3N_4 .

To investigate the surface composition and chemical state of different elements, 10% Ag/mpg- C_3N_4 was analyzed by XPS and the results were shown in Fig. 5. Four elements of C, N, O and Ag are observed in the survey spectrum (Fig. 5a). The C 1s spectrum (Fig. 5b) has four distinct peaks centered at 284.6, 286.4, 288.1 and 293.2 eV, which are assigned to the adventitious carbon (C-C), the sp^3 -hybridized carbon (C-(N) $_3$), the sp^2 -hybridized

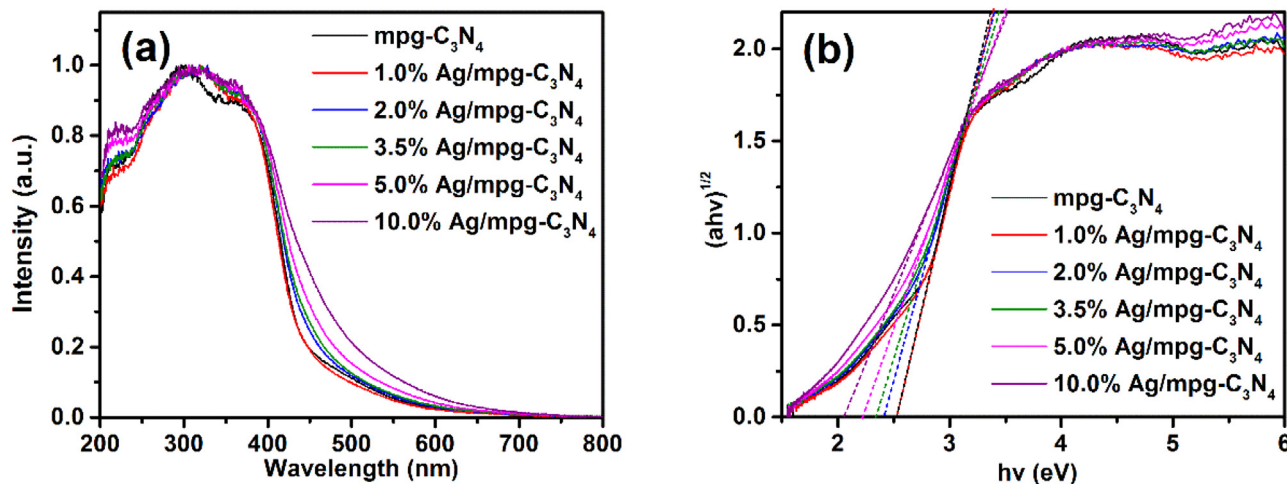


Fig. 4. Diffuse reflectance UV-vis spectra (a) and Tauc plots (b) of Ag/mpg- C_3N_4 with different Ag contents.

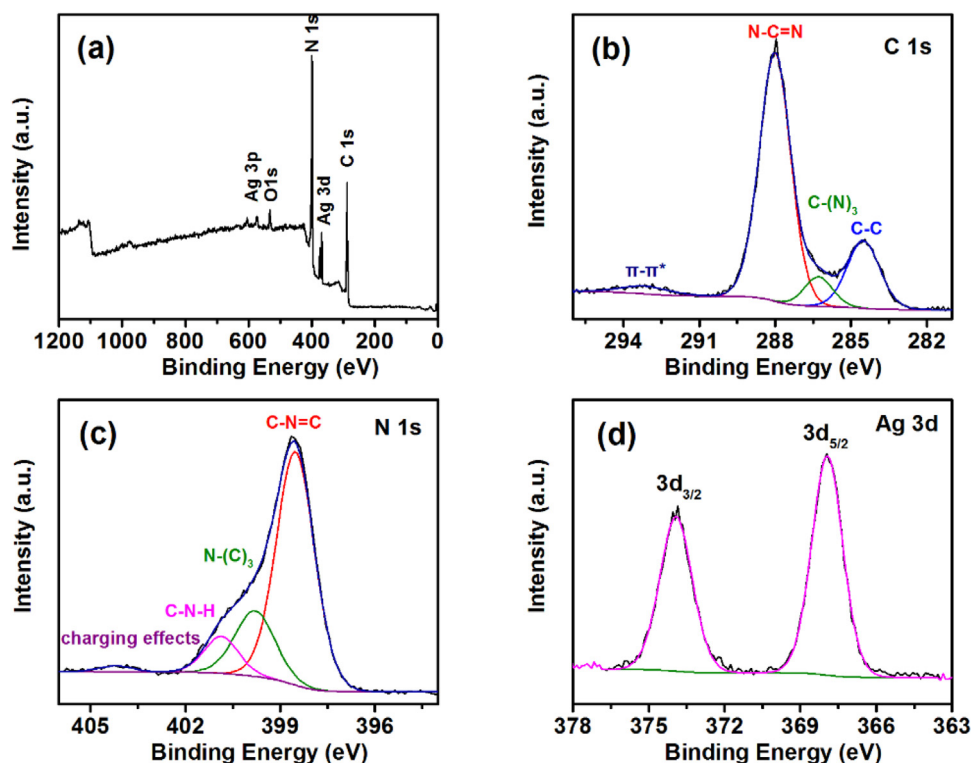


Fig. 5. XPS spectra of 10% Ag/mpg-C₃N₄: survey (a), C 1s (b), N 1s (c), Ag 3d (d).

carbon (N=C=N) [29] and π - π^* . The N 1s spectrum (Fig. 5c) is deconvoluted into four peaks centered at 398.5, 399.8, 400.9 and 404.2 eV, which are assigned to the sp^2 -hybridized nitrogen in aromatic triazine rings (C=C=N), the tertiary nitrogen (N-(C)₃), the free amino groups (C-N-H), and the charging effects or positive charge localization in the heterocycles, respectively [30]. The Ag 3d spectrum (Fig. 5d) presents two individual peaks at about 368.0 and 374.0 eV with 6.0 eV splitting between the two peaks, which corresponds to the metallic Ag⁰ species [17].

3.2. Reactivity and stability of Ag/mpg-C₃N₄

The 10% Ag/mpg-C₃N₄ had no obvious adsorption toward BPA and the degradation of BPA by only PMS was negligible (Fig. S2). As shown in Fig. 6, the removal of BPA catalyzed by g-C₃N₄ in the presence of PMS without irradiation was negligible, indicating the poor reactivity for PMS activation. By contrast, 10% Ag/mpg-C₃N₄ showed the enhanced catalytic activity in the presence of PMS and 15% BPA was removed in 60 min due to the activation of PMS by metallic Ag [31]. The photocatalytic activity of g-C₃N₄ and Ag/mpg-C₃N₄ is also compared under visible light irradiation, and only 2% BPA was removed by g-C₃N₄, which is caused by its poor photocatalytic activity resulting from the rapid recombination of photogenerated electron-hole pairs. In contrast, 43% degradation efficiency of BPA was achieved by 10% Ag/mpg-C₃N₄, which may be caused from the SPR effect. Single-atom Ag can serve as electron sinks to capture photogenerated electrons from the conduction band of g-C₃N₄, which results in a suppression of the charge-recombination process and further promote the photocatalytic activity of 10% Ag/mpg-C₃N₄ [32]. After addition of PMS, BPA degradation is significantly accelerated. It is worth noticing that 98% removal of BPA was achieved in the presence of PMS and 10% Ag/mpg-C₃N₄ under visible light irradiation. And the TOC removal efficiency can achieve 80%. It has been reported that noble metal (i.e., Pd, Pt, Ag and Au) present catalytic activity for PMS activation,

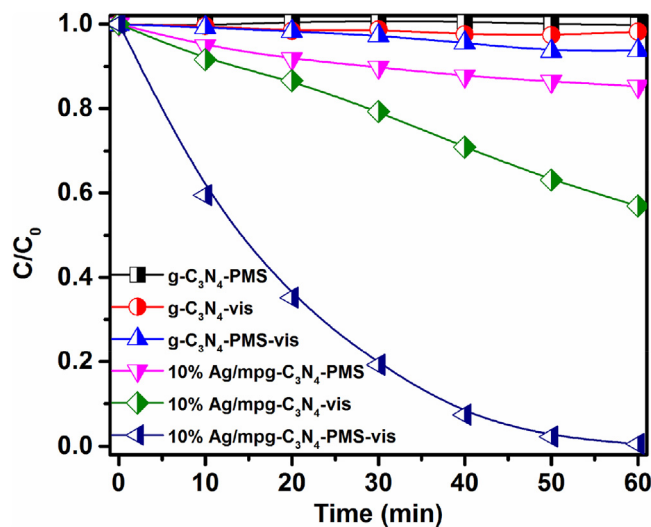


Fig. 6. The degradation of BPA in different systems. Conditions: [BPA]₀ = 20 mg/L, [PMS] = 1 mM and [Cata.] = 0.1 g/L, without buffer.

however, only 6% BPA is removed activated by 10% Ag/mpg-C₃N₄ without visible light irradiation. These results suggested that a synergistic effect exists between single-atom Ag and mpg-C₃N₄ in the photocatalysis system. One possible reason could be that PMS is activated by photogenerated electron to generate SO₄^{•-}.

The effect of other factors, such as Ag contents, PMS concentration, initial pH and anions, on the degradation of BPA by Ag/mpg-C₃N₄/PMS/vis system was investigated. As can be seen from Fig. 7a, the removal efficiency of BPA increases from 88% to 99.4% with Ag contents increasing from 1% to 10%. One possible reason could be that the optical band gap narrows with the increasing Ag contents and the absorption of visible light was enhanced.

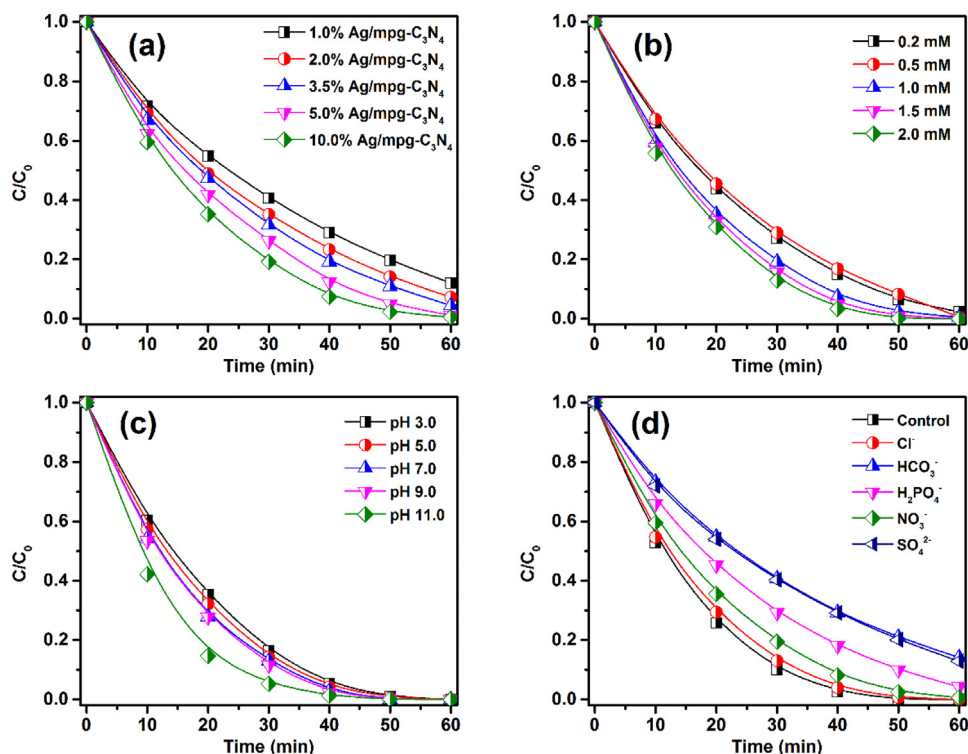


Fig. 7. Influence of Ag contents (a), PMS concentration (b), initial pH (c), and inions (5 mM) on the removal efficiency of BPA. Conditions: $[BPA]_0 = 20 \text{ mg/L}$, $[Cata.] = 0.1 \text{ g/L}$, reaction temperature = 25°C .

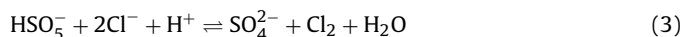
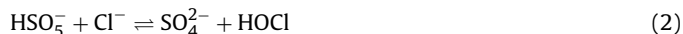
Therefore, more $\text{SO}_4^{\bullet-}$ were generated due to the more produced photogenerated electrons.

In general, the amount of generated $\text{SO}_4^{\bullet-}$ and $\bullet\text{OH}$ relate directly with PMS concentration. Fig. 7b shows the effect of PMS concentration on the degradation of BPA. As we can see, the degradation efficiency of BPA was accelerated when the PMS concentration increased from 0.2 to 1.0 mM. However, no significant additional enhancement for the removal of BPA was observed when the PMS concentration further increased to 2.0 mM. The possible reason could be that the photogenerated electrons are not enough to activate the redundant PMS in 10% Ag/mpg- C_3N_4 /PMS/vis system.

The pH of the medium is a crucial operating parameter as it directly influences the photocatalytic activity. The adsorption of BPA by 10% Ag/mpg- C_3N_4 with different pH values were investigated firstly (Fig. S4), the results showed that the effect of solution pH on the adsorption of BPA is insignificant. It was found that the present photocatalytic process worked effectively over a broad initial pH range from 3.0 to 11.0 and the degradation rate of BPA accelerated when the initial pH increased. However, the differences of BPA degradation rates with initial pH from 3.0 to 9.0 are not obvious, which are possibly due to the acidification of PMS. The solution pH reduced immediately to about 3.0 when 1 mM PMS was added (the data was not shown). It has been reported that the pK_a of PMS is 9.4 [22], therefore, H_2SO_5 is the major form of PMS when the solution pH is lower than 9.4. As a consequence, the activation of PMS is inhibited when the initial $\text{pH} \leq 9$. In contrast, the BPA degradation rate with initial pH 11.0 is higher than others, which is due to the pH decreases slower than others.

In practical operations, many anions such as Cl^- , HCO_3^- , H_2PO_4^- , NO_3^- and SO_4^{2-} , exist in natural water which may affect the removal efficiency of organic pollutants. To eliminate the light shielding effect, UV-vis spectra of BPA solution in the presence of different anions were measured and the results were shown in Fig.S5. As we can see, BPA has two absorption peaks

at 275 and 225 nm, corresponding to $n \rightarrow \pi^*$ and $\pi \rightarrow \pi^*$ transitions [33]. No changes were observed at the visible light region ($\lambda > 400 \text{ nm}$), suggesting the light shielding effect by anions in Ag/mpg- C_3N_4 /PMS/vis system is insignificant. The effect of various inorganic anions on the degradation of BPA was investigated and the results were shown in Fig. 7d. It was found that the effect of anions on the degradation of BPA follows the order of $\text{Cl}^- < \text{NO}_3^- < \text{H}_2\text{PO}_4^- < \text{SO}_4^{2-} \approx \text{HCO}_3^-$. Cl^- has negligible effect on the degradation of BPA, which seems inconsistent with the quenching effect of Cl^- for $\text{SO}_4^{\bullet-}$ ($k_{\text{SO}_4^{\bullet-} + \text{Cl}^-} = 2.0 \times 10^8 \text{ M}^{-1} \text{ s}^{-1}$) [34]. This could be explained by the fact that Cl^- presents the inhibitory effect at low concentrations and shows the acceleration effect when Cl^- is over a critical concentration [35]. According to Eq. (1), Cl^- can react with $\text{SO}_4^{\bullet-}$ to form chloride radicals (Cl^\bullet), whose oxidation potential is lower than $\text{SO}_4^{\bullet-}$. However, a great amount of Cl_2 and HOCl would be generated according to Eqs. (2)–(3).



Although bicarbonate (HCO_3^-) or SO_4^{2-} present the most inhibition for the degradation of BPA, 86% BPA still could be removed in 10% Ag/mpg- C_3N_4 /PMS/vis system within 60 min. As we know, HCO_3^- usually acted as radical scavengers in advanced oxidation processes ($k_{\text{SO}_4^{\bullet-} + \text{HCO}_3^-} = 2.8 \times 10^6 \text{ M}^{-1} \text{ s}^{-1}$). Therefore, the inhibition for the degradation of BPA by HCO_3^- may be due to its competing reaction with PMS. Phosphate ions ($\text{HPO}_4^{2-}/\text{H}_2\text{PO}_4^-$) have a similar quench effect with $\text{CO}_3^{2-}/\text{HCO}_3^-$ on $\text{SO}_4^{\bullet-}$ and/or $\bullet\text{OH}$. However, the inhibition of SO_4^{2-} is not clear and deserves further research.

Cycling tests were conducted to estimate the stability of the as-prepared 10% Ag/mpg- C_3N_4 in the presence of PMS and the results were presented in Fig. 8. As we can see, the catalytic performance

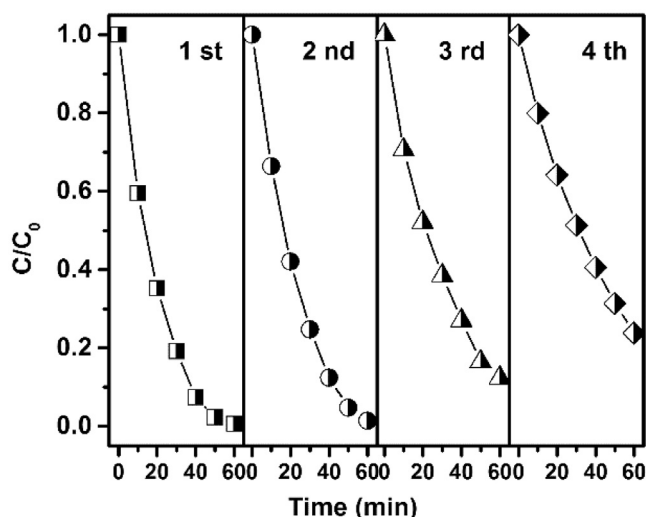


Fig. 8. Cycling test of 10% Ag/mpg-C₃N₄/PMS for the degradation of BPA.

of 10% Ag/mpg-C₃N₄ is gradually decreased, which may result from the block of active sites by the degradation intermediates of BPA. However, 76% of BPA still can be removed after four successive cycling tests, indicating the good stability of Ag/mpg-C₃N₄.

3.3. Photoelectrochemical property

To further understand the role of the single-atom Ag in photocatalysis, photoelectrochemical properties were investigated. Fig. 9a displays the photocurrent response of different photocat-

alysts at 0V (vs. SCE). The transient photocurrent of g-C₃N₄ was observed, and the photocurrent significantly enhanced for 5%- and 10% Ag/mpg-C₃N₄, suggesting the introduction of Ag into mpg-C₃N₄ effectively suppress the recombination of photogenerated electron-hole pairs. To understand the role of PMS in the photocatalytic process, LSV curves were measured in the presence or absence of PMS, and the results were shown in Fig. 9b. As we can see, the current of 10% Ag/mpg-C₃N₄ under visible light irradiation is slightly higher than that of dark condition. However, the current significantly enhanced in the presence of PMS both in the dark and under the irradiation of visible light. This phenomenon demonstrates that the interplay occurred between 10% Ag/mpg-C₃N₄ and PMS and the photogenerated electrons transfer from 10% Ag/mpg-C₃N₄ to PMS. In the system of 10% Ag/mpg-C₃N₄/PMS/vis, PMS acted as electron acceptor.

Electrochemical impedance spectroscopy (EIS) Nyquist plots of g-C₃N₄ and 10% Ag/mpg-C₃N₄ were shown in Fig. 10a. Because the preparation of the electrodes and electrolyte used are identical, the high frequency semicircle is related to the resistance of the electrode. In EIS Nyquist plots, the high frequency arc corresponds to the double-layer capacitance (C_{dl}) in parallel with the charge transfer resistance (R_{ct}) at the contact interface between the electrode and electrolyte solution [36]. As shown in Fig. 10a, the arc radius on the EIS Nyquist plot of 10% Ag/mpg-C₃N₄ is smaller than that of g-C₃N₄ in the case of both with and without visible light irradiation. This suggests that the former owns a more effective separation of photogenerated electron-hole pairs and faster interfacial charge transfer.

The Mott-Schottky (M-S) plots of g-C₃N₄ and 10% Ag/mpg-C₃N₄ were measured at 100 Hz in the dark to determine the nature of the semiconductor and the flat band potential (V_{FB}) were evalu-

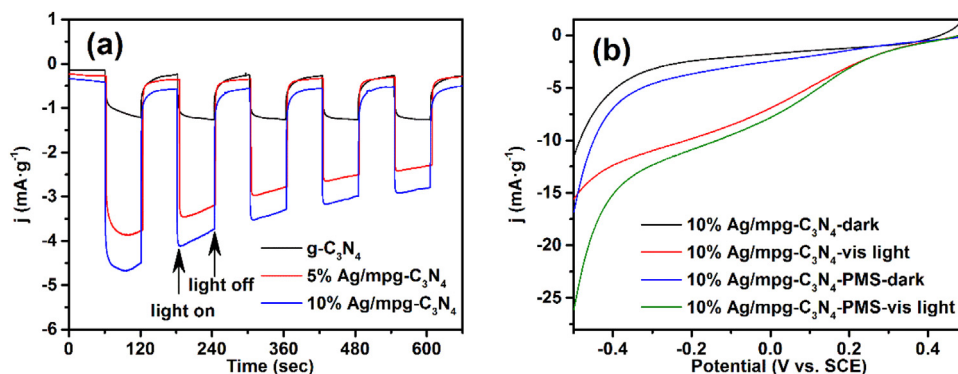


Fig. 9. Transient photocurrent response of different photocatalysts at bias 0V (vs. SCE) (a) and LSV curves in the presence or absence of 1.0 mM PMS (b). Conditions: 50 mM Na₂SO₄, $\lambda > 400$ nm.

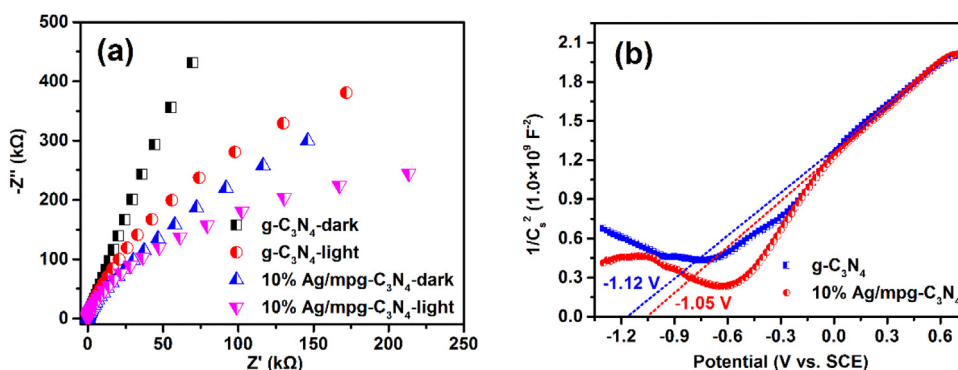


Fig. 10. EIS Nyquist with or without visible light irradiation (a) and Mott-Schottky plots measured at a frequency of 100 Hz in the dark (b) of g-C₃N₄ and 10% Ag/mpg-C₃N₄. Conditions: $\lambda > 400$ nm, 50 mM PBS with pH 7.0.

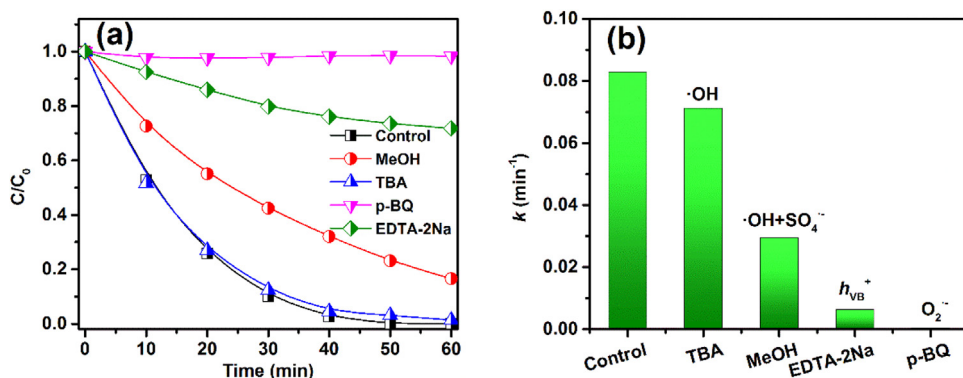


Fig. 11. The degradation of BPA (a) and corresponding pseudo-first order constants (b) in the presence of different scavengers. Conditions: $[BPA]_0 = 20$ mg/L, $[PMS] = 1$ mM, $[Cata.] = 0.1$ g/L, $[MeOH] = [TBA] = 1$ M, $[EDTA-2Na] = [p-BQ] = 12$ mM, reaction temperature = 25°C .

ated from the x-intercept of the M-S plot. The V_{FB} is approximately equal to the conduction band edge potential (V_{CB}) or the valence band edge potential (V_{VB}) in the case of an n-type or a p-type semiconductor, respectively [37]. As shown in Fig. 10b, the positive slope of the plots revealed that the n-type semiconductor feature of the g-C₃N₄ and 10% Ag/mpg-C₃N₄. Therefore, the calculated V_{FB} of g-C₃N₄ and 10% Ag/mpg-C₃N₄ are -1.12 and -1.05 V (vs. SCE), corresponding to -0.88 and -0.81 V (vs. NHE), respectively. This means that the V_{CB} of g-C₃N₄ and 10% Ag/mpg-C₃N₄ were significantly more negative than the redox potential of $SO_4^{\bullet-}/SO_4^{2-}$ ($2.5-3.1$ V vs. NHE) [38], satisfying the thermodynamic requirements for the activation of PMS by photogenerated electrons under visible light irradiation, and generated $SO_4^{\bullet-}$. According to their optical band gap, the V_{VB} of g-C₃N₄ and 10% Ag/mpg-C₃N₄ are 1.82 and 1.28 V (vs. NHE), respectively, which are lower than the redox potential of $\bullet OH/OH^-$ (2.38 V vs. NHE) [38]. Thus, the photogenerated holes in 10% Ag/mpg-C₃N₄ is unable to oxidize OH^- to generate $\bullet OH$.

3.4. Proposed mechanism

The ROS and photogenerated electrons-holes maybe involved in the photocatalytic degradation of BPA in Ag/mpg-C₃N₄/PMS/vis system. Therefore, competitive radical tests were performed to identify the contribution of each ROS for BPA degradation. Methanol (MeOH) was used to scavenge both $\bullet OH$ ($k = 9.7 \times 10^8 \text{ M}^{-1} \text{ s}^{-1}$) and $SO_4^{\bullet-}$ ($k = 2.5 \times 10^7 \text{ M}^{-1} \text{ s}^{-1}$) [39,40]. And *tert*-butyl alcohol (TBA) was used to scavenge $\bullet OH$ ($k = 3.8-7.6 \times 10^8 \text{ M}^{-1} \text{ s}^{-1}$) [39], because TBA reacts with $SO_4^{\bullet-}$ ($k = 4.0-9.1 \times 10^5 \text{ M}^{-1} \text{ s}^{-1}$) [40] over 1000-fold lower than $\bullet OH$. EDTA-2Na and *p*-benzoquinone (*p*-BQ) were used as hole (h_{VB}^+) and superoxide radical ($O_2^{\bullet-}$) scavengers, respectively. As can be seen in Fig. 11b, the inhibition performance for the degradation of BPA follows the order $p\text{-BQ} > \text{EDTA-2Na} > \text{MeOH} > \text{TBA}$, indicating that $O_2^{\bullet-}$, h_{VB}^+ , $SO_4^{\bullet-}$ and $\bullet OH$ are responsible for the degradation of BPA. Of which, the role of $\bullet OH$ is limited, while $SO_4^{\bullet-}$, $O_2^{\bullet-}$ and h_{VB}^+ are the major oxidized species in Ag/mpg-C₃N₄/PMS/vis system.

To further validate the ROS in Ag/mpg-C₃N₄/PMS/vis system, ESR experiments using 5-*tert*-Butoxycarbonyl-5-methyl-1-pyrroline-*N*-oxide (BMPO) as a radical spin trapping agent were performed. As seen in Fig. 12, seven-line spectra (hyperfine splitting constants $a_N = 7.35$ G, $a_H^\beta = 3.65$ G and $a_H^\gamma = 3.65$ G) were observed, which may be assigned to 5-*tert*-Butoxycarbonyl-5-methyl-2-oxopyrroline-1-oxyl (BMPOX), which is similar with the reported DMPOX [41]. In contrast, no BMPO-OH or BMPO- SO_4 adducts are observed. For 10% Ag/mpg-C₃N₄, the intensity of BMPOX signal enhances at 5 min and then diminishes at 10 min. In term of g-C₃N₄, a similar tendency is observed, but the relative intensity is

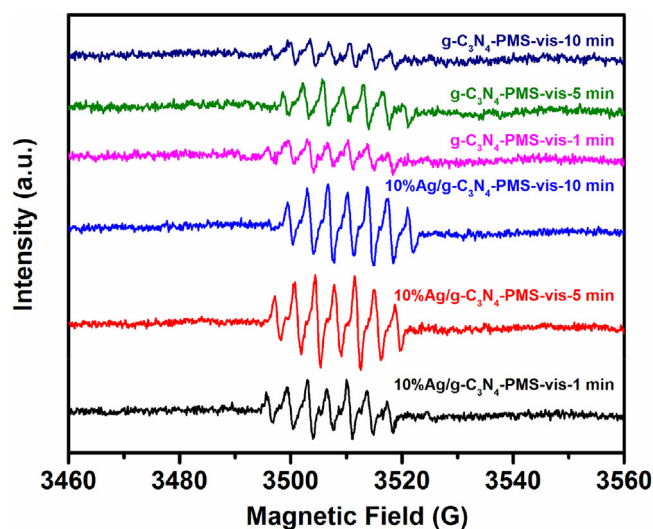
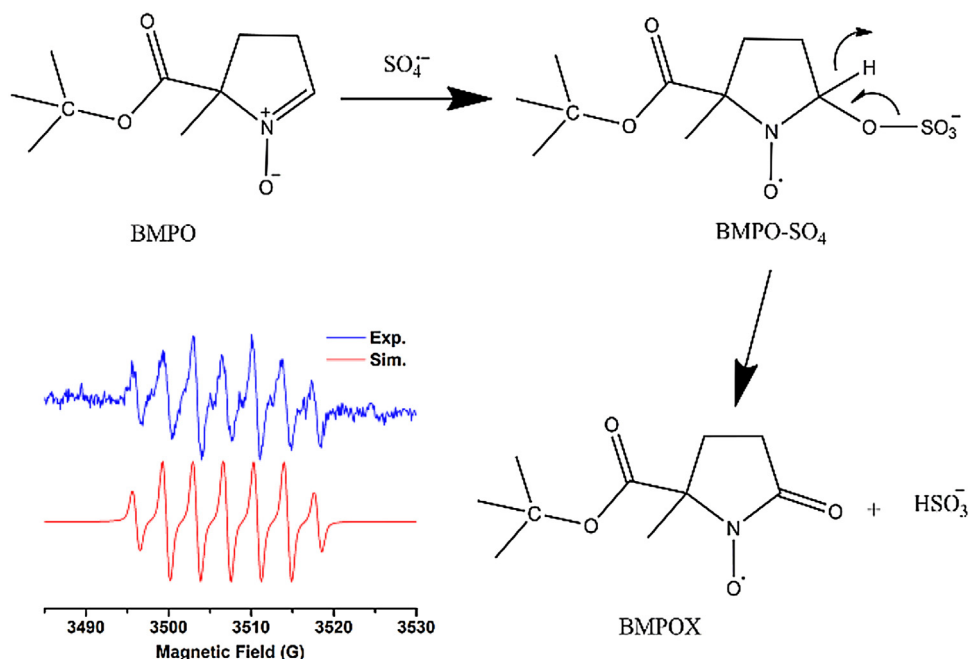


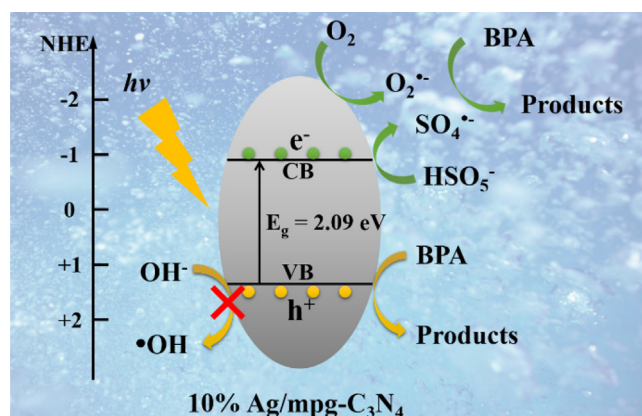
Fig. 12. ESR spectra of g-C₃N₄ and 10% Ag/mpg-C₃N₄ as photocatalysts in the presence of PMS under visible light irradiation. Conditions: $[Cata.] = 0.1$ g/L, $[PMS] = 1$ mM, $[BMPO] = 25$ mM, $\lambda > 400$ nm.

lower than that of 10% Ag/mpg-C₃N₄. BMPOX might come from the reaction of BMPO with $SO_4^{\bullet-}$ radicals. As we know, the DMPO- SO_4 adduct is difficult to detect because of its low sensitivity and short life-time [42]. Thus, the BMPOX peak can be originated from the BMPO- SO_4 adduct, as shown in Scheme 1 [43].

Based on the above results, a plausible mechanism for the degradation of BPA in Ag/mpg-C₃N₄/PMS/vis system is proposed and shown in Scheme 2. Owing to the introduction of single-atom Ag, the visible light harvesting ability of Ag/mpg-C₃N₄ is improved due to SPR absorption of single-atom Ag. Thus, more photoinduced electrons (e_{CB}^-) and holes (h_{VB}^+) are generated (Eq. (4)) in Ag/mpg-C₃N₄ under the visible light irradiation. The SPR effect of single-atom Ag can induce enhancement of the local electromagnetic field, which can speed the generation rate of e_{CB}^- and h_{VB}^+ [44]. In addition, a Schottky barrier is created due to the matched energy level of Ag and g-C₃N₄, hence, the recombination of e_{CB}^- and h_{VB}^+ is minimized. In the presence of PMS, the e_{CB}^- could be trapped by PMS to produce $SO_4^{\bullet-}$ (Eq. (5)), then the separation efficiency of electrons and holes are promoted. In addition, e_{CB}^- reacts with O_2 to form $O_2^{\bullet-}$ (Eq. (6)), which combines with h_{VB}^+ to oxidize BPA molecular (Eq. (7)). As for $\bullet OH$, the V_{CB} of Ag/mpg-C₃N₄ is lower than the redox of $\bullet OH/OH^-$, thus the generated h_{VB}^+ could not oxidize OH^- to generate $\bullet OH$. In addition, the pH decreases quickly to about 3 with the addition of PMS, and the generation of $\bullet OH$ from the reaction between $SO_4^{\bullet-}$ and OH^- is inhibited. In sum-

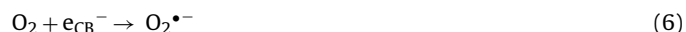
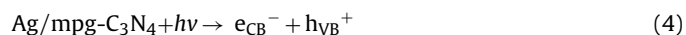


Scheme 1. The proposed mechanism for the formation of BMPOX.



Scheme 2. The possible photocatalytic mechanism in Ag/mpg-C₃N₄/PMS/vis system.

mary, O₂•⁻, SO₄•⁻ and h_{VB}⁺ are the major oxidizing species, while the contribution of •OH for the degradation of BPA is insignificant.



4. Conclusions

Single-atom dispersed Ag/mpg-C₃N₄ hybrid was employed as visible light responded photocatalyst. In the presence of PMS, the degradation efficiency of BPA was significant enhanced owing to the synergistic effect of metallic Ag and mpg-C₃N₄. Photoelectrochemical tests revealed that the separation efficiency of photogenerated electrons-holes was enhanced. ESR and free radicals quenching experiment indicated that SO₄•⁻, O₂•⁻ and holes were the major oxidizing species. In Ag/mpg-C₃N₄/PMS/vis system, PMS functions as an acceptor of photogenerated electrons and was activated by electrons to form SO₄•⁻.

Acknowledgements

This work was supported by the National Natural Science Foundation P.R. China (Project Nos. 21377148, 51222802). We appreciate the anonymous reviewers' valuable revision suggestions.

Appendix A. Supplementary data

Supplementary data associated with this article can be found, in the online version, at <http://dx.doi.org/10.1016/j.apcatb.2017.03.079>.

References

- [1] J. Liu, Y. Liu, N.Y. Liu, Y.Z. Han, X. Zhang, H. Huang, Y. Lifshitz, S.T. Lee, J. Zhong, Z.H. Kang, Metal-free efficient photocatalyst for stable visible water splitting via a two-electron pathway, *Science* 347 (2015) 970–974.
- [2] X.C. Wang, K. Maeda, A. Thomas, K. Takanabe, G. Xin, J.M. Carlsson, K. Domen, M. Antonietti, A metal-free polymeric photocatalyst for hydrogen production from water under visible light, *Nat. Mater.* 8 (2009) 76–80.

- [3] P. Niu, L.L. Zhang, G. Liu, H.M. Cheng, Graphene-like carbon nitride nanosheets for improved photocatalytic activities, *Adv. Funct. Mater.* 22 (2012) 4763–4770.
- [4] K. Wang, Q. Li, B.S. Liu, B. Cheng, W.K. Ho, J.G. Yu, Sulfur-doped g-C₃N₄ with enhanced photocatalytic CO₂-reduction performance, *Appl. Catal. B: Environ.* 176 (2015) 44–52.
- [5] P. Niu, Y.Q. Yang, J.C. Yu, G. Liu, H.M. Cheng, Switching the selectivity of the photoreduction reaction of carbon dioxide by controlling the band structure of a g-C₃N₄ photocatalyst, *Chem. Commun.* 50 (2014) 10837–10840.
- [6] C. Liu, L.Q. Jing, L.M. He, Y.B. Luan, C.M. Li, Phosphate-modified graphitic C₃N₄ as efficient photocatalyst for degrading colorless pollutants by promoting O₂ adsorption, *Chem. Commun.* 50 (2014) 1999–2001.
- [7] H. Zhang, L.H. Guo, L.X. Zhao, B. Wan, Y. Yang, Switching oxygen reduction pathway by exfoliating graphitic carbon nitride for enhanced photocatalytic phenol degradation, *J. Phys. Chem. Lett.* 6 (2015) 958–963.
- [8] Y. Shiraishi, S. Kanazawa, Y. Kofuji, H. Sakamoto, S. Ichikawa, S. Tanaka, T. Hirai, Sunlight-driven hydrogen peroxide production from water and molecular oxygen by metal-free photocatalysts, *Angew. Chem. Int. Ed.* 53 (2014) 13454–13459.
- [9] Y. Shiraishi, S. Kanazawa, Y. Sugano, D. Tsukamoto, H. Sakamoto, S. Ichikawa, T. Hirai, Highly selective production of hydrogen peroxide on graphitic carbon nitride (g-C₃N₄) photocatalyst activated by visible light, *ACS Catal.* 4 (2014) 774–780.
- [10] Y. Shiraishi, Y. Kofuji, H. Sakamoto, S. Tanaka, S. Ichikawa, T. Hirai, Effects of surface defects on photocatalytic H₂O₂ production by mesoporous graphitic carbon nitride under visible light irradiation, *ACS Catal.* 5 (2015) 3058–3066.
- [11] F. Raziq, C.M. Li, M. Humayun, Y. Qu, A. Zada, H.T. Yu, L.Q. Jing, Synthesis of TiO₂/g-C₃N₄ nanocomposites as efficient photocatalysts dependent on the enhanced photogenerated charge separation, *Mater. Res. Bull.* 70 (2015) 494–499.
- [12] Y. Zhang, Q. Wang, J.N. Lu, Q. Wang, Y.Q. Cong, Synergistic photoelectrochemical reduction of Cr(VI) and oxidation of organic pollutants by g-C₃N₄/TiO₂-NTs electrodes, *Chemosphere* 162 (2016) 55–63.
- [13] S.C. Yan, Z.S. Li, Z.G. Zou, Photodegradation of Rhodamine B and Methyl Orange over boron-doped g-C₃N₄ under visible light irradiation, *Langmuir* 26 (2010) 3894–3901.
- [14] G.H. Dong, K. Zhao, L.Z. Zhang, Carbon self-doping induced high electronic conductivity and photoreactivity of g-C₃N₄, *Chem. Commun.* 48 (2012) 6178–6180.
- [15] J.D. Hong, X.Y. Xia, Y.S. Wang, R. Xu, Mesoporous carbon nitride with in situ sulfur doping for enhanced photocatalytic hydrogen evolution from water under visible light, *J. Mater. Chem.* 22 (2012) 15006–15012.
- [16] J.H. Li, B.A. Shen, Z.H. Hong, B.Z. Lin, B.F. Gao, Y.L. Chen, A facile approach to synthesize novel oxygen-doped g-C₃N₄ with superior visible-light photoreactivity, *Chem. Commun.* 48 (2012) 12017–12019.
- [17] S.L. Ma, S.H. Zhan, Y.N. Jia, Q. Shi, Q.X. Zhou, Enhanced disinfection application of Ag-modified g-C₃N₄ composite under visible light, *Appl. Catal. B: Environ.* 186 (2016) 77–87.
- [18] G.H. Dong, L.P. Yang, F. Wang, L. Zang, C.Y. Wang, Removal of nitric oxide through visible light photocatalysis by g-C₃N₄ modified with perylene imides, *ACS Catal.* 6 (2016) 6511–6519.
- [19] X.G. Li, W.T. Bi, L. Zhang, S. Tao, W.S. Chu, Q. Zhang, Y. Luo, C.Z. Wu, Y. Xie, Single-atom Pt as co-catalyst for enhanced photocatalytic H₂ evolution, *Adv. Mater.* 28 (2016) 2427–2431.
- [20] G.P. Gao, Y. Jiao, E.R. Wacławik, A.J. Du, Single atom (Pd/Pt) supported on graphitic carbon nitride as an efficient photocatalyst for visible-light reduction of carbon dioxide, *J. Am. Chem. Soc.* 138 (2016) 6292–6297.
- [21] Z.P. Chen, S. Pronkin, T.P. Fellinger, K. Kailasam, G. Vile, D. Albani, F. Krumeich, R. Leary, J. Barnard, J.M. Thomas, J. Perez-Ramirez, M. Antonietti, D. Dontsova, Merging single-atom-dispersed silver and carbon nitride to a joint electronic system via copolymerization with silver tricyanomethanide, *ACS Nano* 10 (2016) 3166–3175.
- [22] P.D. Hu, M.C. Long, Cobalt-catalyzed sulfate radical-based advanced oxidation: a review on heterogeneous catalysts and applications, *Appl. Catal. B: Environ.* 181 (2016) 103–117.
- [23] Y. Feng, D.L. Wu, Y. Deng, T. Zhang, K.M. Shih, Sulfate radical-mediated degradation of sulfadiazine by CuFeO₂ rhombohedral crystal-catalyzed peroxymonosulfate: synergistic effects and mechanisms, *Environ. Sci. Technol.* 50 (2016) 3119–3127.
- [24] Y.W. Gao, S.M. Li, Y.X. Li, L.Y. Yao, H. Zhang, Accelerated photocatalytic degradation of organic pollutant over metal-organic framework MIL-53(Fe) under visible LED light mediated by persulfate, *Appl. Catal. B: Environ.* 202 (2017) 165–174.
- [25] H.T. Ren, S.Y. Jia, Y. Wu, S.H. Wu, T.H. Zhang, X. Han, Improved photochemical reactivities of Ag₂O/g-C₃N₄ in phenol degradation under UV and visible light, *Ind. Eng. Chem. Res.* 53 (2014) 17645–17653.
- [26] D.L. Jiang, J.J. Zhu, M. Chen, J.M. Xie, Highly efficient heterojunction photocatalyst based on nanoporous g-C₃N₄ sheets modified by Ag₃PO₄ nanoparticles: synthesis and enhanced photocatalytic activity, *J. Colloid Interface Sci.* 417 (2014) 115–120.
- [27] Y.X. Yang, Y.N. Guo, F.Y. Liu, X. Yuan, Y.H. Guo, S.Q. Zhang, W. Guo, M.X. Huo, Preparation and enhanced visible-light photocatalytic activity of silver deposited graphitic carbon nitride plasmonic photocatalyst, *Appl. Catal. B: Environ.* 142 (2013) 828–837.
- [28] Y.P. Bi, H.Y. Hu, S.X. Ouyang, Z.B. Jiao, G.X. Lu, J.H. Ye, Selective growth of Ag₃PO₄ submicro-cubes on Ag nanowires to fabricate necklace-like heterostructures for photocatalytic applications, *J. Mater. Chem.* 22 (2012) 14847–14850.
- [29] J.D. Xiao, Y.B. Xie, F. Nawaz, Y.X. Wang, P.H. Du, H.B. Cao, Dramatic coupling of visible light with ozone on honeycomb-like porous g-C₃N₄ towards superior oxidation of water pollutants, *Appl. Catal. B: Environ.* 183 (2016) 417–425.
- [30] B.H. Long, J.L. Lin, X.C. Wang, Thermally-induced desulfurization and conversion of guanidine thiocyanate into graphitic carbon nitride catalysts for hydrogen photosynthesis, *J. Mater. Chem. A* 2 (2014) 2942–2951.
- [31] Y.Y. Ahn, E.T. Yun, J.W. Seo, C. Lee, S.H. Kim, J.H. Kim, J. Lee, Activation of peroxymonosulfate by surface-loaded noble metal nanoparticles for oxidative degradation of organic compounds, *Environ. Sci. Technol.* 50 (2016) 10187–10197.
- [32] S.W. Cao, J.X. Low, J.G. Yu, M. Jaroniec, Polymeric photocatalysts based on graphitic carbon nitride, *Adv. Mater.* 27 (2015) 2150–2176.
- [33] T. Soltani, B.K. Lee, Sono-synthesis of nanocrystallized BiFeO₃/reduced graphene oxide composites for visible photocatalytic degradation improvement of bisphenol A, *Chem. Eng. J.* 306 (2016) 204–213.
- [34] H.V. Lutz, N. Kerlin, T.C. Schmidt, Sulfate radical-based water treatment in presence of chloride: formation of chlorate, inter-conversion of sulfate radicals into hydroxyl radicals and influence of bicarbonate, *Water Res.* 72 (2015) 349–360.
- [35] R.X. Yuan, S.N. Ramjaun, Z.H. Wang, J.S. Liu, Effects of chloride ion on degradation of Acid Orange 7 by sulfate radical-based advanced oxidation process: implications for formation of chlorinated aromatic compounds, *J. Hazard. Mater.* 196 (2011) 173–179.
- [36] X.J. Bai, L. Wang, Y.J. Wang, W.Q. Yao, Y.F. Zhu, Enhanced oxidation ability of g-C₃N₄ photocatalyst via C-60 modification, *Appl. Catal. B: Environ.* 152 (2014) 262–270.
- [37] A. Mitra, P. Howli, D. Sen, B. Das, K.K. Chattopadhyay, Cu₂O/g-C₃N₄ nanocomposites: an insight into the band structure tuning and catalytic efficiencies, *Nanoscale* 8 (2016) 19099–19109.
- [38] G.P. Anipsitakis, D.D. Dionysiou, Degradation of organic contaminants in water with sulfate radicals generated by the conjunction of peroxymonosulfate with cobalt, *Environ. Sci. Technol.* 37 (2003) 4790–4797.
- [39] G.V. Buxton, C.L. Greenstock, W.P. Helman, A.B. Ross, Critical-review of rate constants for reactions of hydrated electrons, hydrogen-atoms and hydroxyl radicals (OH/O⁻) in aqueous-solution, *J. Phys. Chem. Ref. Data* 17 (1988) 513–886.
- [40] P. Neta, R.E. Huie, A.B. Ross, Rate constants for reactions of inorganic radicals in aqueous-solution, *J. Phys. Chem. Ref. Data* 17 (1988) 1027–1284.
- [41] S.D. Stan, M.A. Daeschel, 5,5-Dimethyl-2-pyrrolidone-N-oxyl formation in electron spin resonance studies of electrolyzed NaCl solution using 5,5-dimethyl-1-pyrroline-N-oxide as a spin trapping agent, *J. Agric. Food Chem.* 53 (2005) 4906–4910.
- [42] K. Rangelova, A.B. Rice, A. Khajo, M. Triquigneaux, S. Garantziotis, R.S. Magliozzo, R.P. Mason, Formation of reactive sulfite-derived free radicals by the activation of human neutrophils: an ESR study, *Free Radic. Biol. Med.* 52 (2012) 1264–1271.
- [43] S. Maeno, Q.Q. Zhu, M. Sasaki, T. Miyamoto, M. Fukushima, Monopersulfate oxidation of tetrabromobisphenol A by an iron(III)-phthalocyaninetetrasulfate catalyst coordinated to imidazole functionalized silica particles, *J. Mol. Catal. A-Chem.* 400 (2015) 56–63.
- [44] J. Qin, H. Zeng, Photocatalysts fabricated by depositing plasmonic Ag nanoparticles on carbon quantum dots/graphitic carbon nitride for broad spectrum photocatalytic hydrogen generation, *Appl. Catal. B: Environ.* 209 (2017) 161–173.